Industrial Chemistry
& Materials

PAPER

View Article Online
View Journal

Cite this: DOI: 10.1039/d6im00074f

Chiral recognition and efficient enantiopurification of L-lactic acid by diastereomeric crystallization

Yuanyuan Shen,[a] Ying Liu,*[a] Zexiang Ding,[a] Jiaqi Li,[a] Rundao Chen,[a] Feng Zhou,[b] Lihang Chen,[c] Qimei Sun,[b] Yuli Bai,[b] Zhiguo Zhang,[ac] Qiwei Yang,[ac] Kai Qiao,[b] Qilong Ren[ac] and Zongbi Bao*[ac]

The production of high-performance polylactic acid (PLA) with tailored thermomechanical properties is critically dependent on the enantiomeric purity of its L-lactic acid (L-LA) precursor. Current industrial processes often yield low-grade L-LA streams (around 80% *ee*) due to racemization during lactide formation, leading to substantial material loss and limiting the widespread adoption of high-stereoregularity PLA. Herein, we report on a highly efficient and industrially viable diastereomeric crystallization strategy for the upgrading of L-LA. Our method leverages the selective formation of crystalline salts between L-LA and specific chiral aromatic amines. Systematic screening identified (*R*)-1-phenylpropylamine ((*R*)-1-PA) and (*R*)-1-phenylethylamine ((*R*)-1-PEA) as superior resolving agents, enabling the crystallization of L-LA in acetonitrile (MeCN) with exceptional enantiomeric excess (*ee* ≥ 99% and ≥ 97%, respectively) and high yields (70% and 68%). Single-crystal X-ray diffraction (SCXRD) reveals pronounced structural divergence among the corresponding diastereomeric salts, including distinct hydrogen-bonding networks and π–π stacking arrangements. Combined thermochemical analysis, phase-equilibrium studies, and molecular simulations demonstrate that chiral recognition arises from the cooperative interplay of electrostatic complementarity, directional hydrogen bonding, and multivalent aromatic interactions. Leveraging these insights, we establish an integrated reaction-crystallization-distillation process that upgrades low-grade L-LA to high-purity feedstock with efficient recovery and recycling of both solvent and resolving agent. This work presents an industrially viable crystallization-based purification strategy, offering a practical solution for enhancing the stereoregularity, performance, and industrial applicability of PLA, thereby addressing a key bottleneck in the sustainable polymer industry.

Received 26th February 2026,
Accepted 5th May 2026

DOI: 10.1039/d6im00074f

rsc.li/icm

Keywords: Polylactic acid; L-lactic acid; Chiral recognition; Diastereomeric crystallization; Aromatic amine.

1 Introduction

Polylactic acid (PLA), a renewable and biodegradable polymer, has emerged as a strategic alternative to mitigate global plastic pollution and advance carbon neutrality.[1,2] The PLA market has experienced rapid growth in recent years, with a compound annual growth rate exceeding 15%, and its applications have expanded into high-value sectors, including advanced packaging, biomedical implants, and engineering plastics.[3–5] However, the thermomechanical performance of PLA is strongly determined by its stereoregularity, which critically depends on the enantiomeric excess (*ee*) of its precursor L-lactic acid (L-LA). Specifically, the *ee* of L-LA must generally exceed 97% to achieve optimal polymer properties.[6] In the industrial route based on lactide ring-opening polymerization (ROP), L-LA is first cyclized to lactide and subsequently purified. However, the high temperatures and catalytic conditions readily induce racemization, yielding approximately 6–20% stereochemically impure *meso*-lactide (*m*-lactide) (Fig. 1a). During the ensuing ROP, these stereochemical defects are incorporated into the polymer backbone as D-configured units, giving rise to so-called "low-grade lactic acid" streams (L-LA : D-LA = 9 : 1, mol). In conventional processes, such streams are typically regarded as unusable byproducts and discarded, leading to substantial material loss. Even at trace levels, the incorporation of

---

[a] Key Laboratory of Biomass Chemical Engineering of Ministry of Education, College of Chemical and Biological Engineering, Zhejiang University, Hangzhou 310058, Zhejiang, P. R. China. E-mail: liuying_ly@zju.edu.cn, baozb@zju.edu.cn
[b] SINOPEC Dalian Research Institute of Petroleum and Petrochemicals Co., Ltd., Dalian 116045, Liaoning, P. R. China
[c] Institute of Zhejiang University-Quzhou, Quzhou 324000, Zhejiang, P. R. China

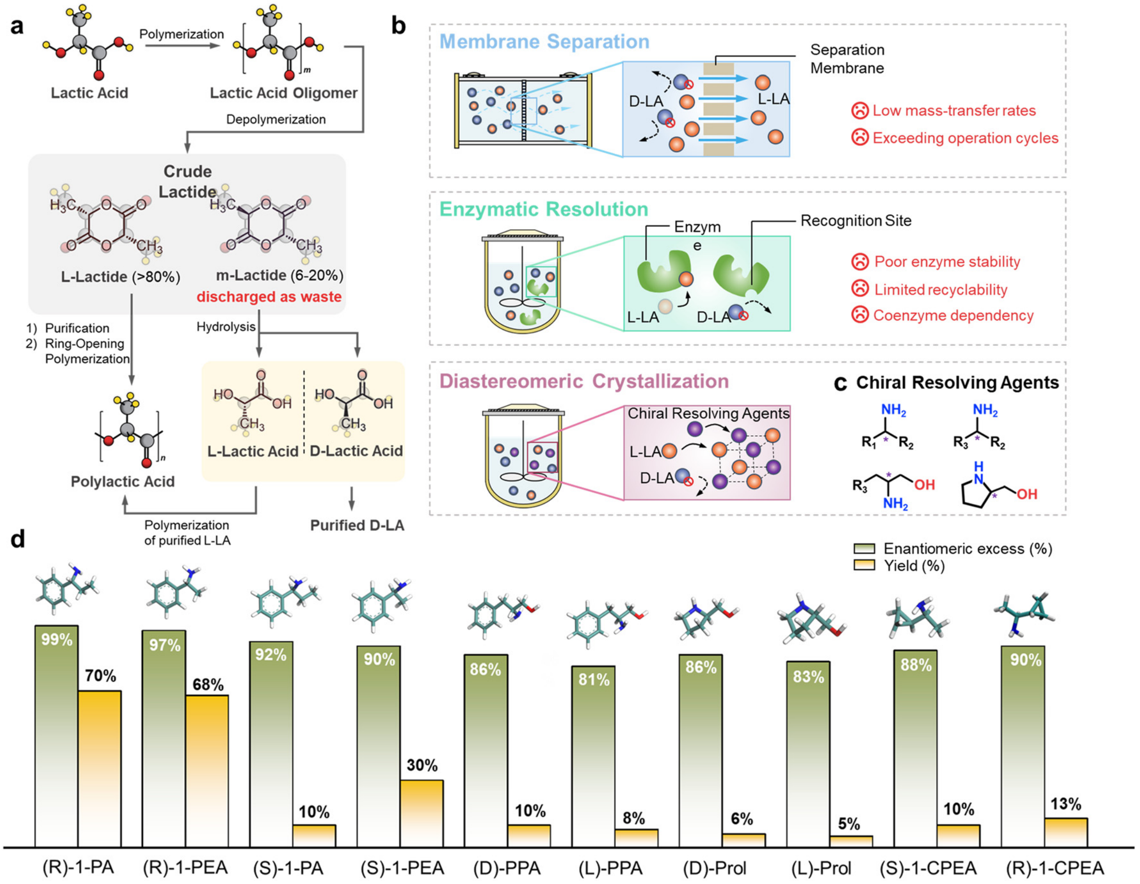

Fig. 1 (a) The production process of polylactic acid from lactic acid, and the racemization pathways during lactide synthesis; (b) current separation strategies and their limitations; (c) classification of chiral resolving agents employed in diastereomeric crystallization. R_1 = alkyl, R_2 = cycloalkyl, R_3 = aryl; * denotes the chiral center; (d) structures of selected chiral resolving agents, and comparison of enantiomeric excess and crystallization yield for L-LA purified using different chiral resolving agents *via* diastereomeric crystallization. Low-grade L-LA (80% *ee*) was used as the starting material. (*R*)-1-PA = (*R*)-1-phenylpropylamine, (*R*)-1-PEA = (*R*)-1-phenylethylamine, (*S*)-1-PA = (*S*)-1-phenylpropylamine, (*S*)-1-PEA = (*S*)-1-phenylethylamine, (D)-PPA = (D)-phenylalaninol; (L)-PPA = (L)-phenylalaninol; (D)-Prol = (D)-Prolinol; (L)-Prol = (L)-Prolinol; (*S*)-1-CPEA = (*S*)-1-cyclopropylethylamine; (*R*)-1-CPEA = (*R*)-1-cyclopropylethylamine.

D-units disrupts regular chain packing, reducing crystallinity, glass transition temperature, and melting point, thereby compromising mechanical strength and thermal stability.[7,8] Therefore, the purification of crude products containing *m*-lactide not only recovers material that would otherwise be discarded, but also enables the full reutilization of low-grade lactic acid. This strategy significantly enhances PLA stereoregularity and thermal properties while minimizing raw material waste, lowering production costs, and improving industrial feasibility.

The separation of lactic acid enantiomers remains a formidable challenge due to their nearly identical physicochemical properties, which limits the efficacy of conventional techniques like distillation and solvent extraction.[9,10] The two primary alternatives-membrane separation and enzymatic resolution-each exhibit considerable limitations (Fig. 1b). Membrane-based separations are impeded by intrinsically low mass-transfer rates and operation cycles exceeding 300 hours, failing to meet industrial throughput requirements.[11] Meanwhile, enzymatic pathways, despite their high enantioselectivity, are constrained by poor enzyme stability, limited recyclability, and cofactor dependency.[12] These limitations underscore an urgent demand for advanced separation methods that combine high selectivity with high productivity to facilitate the scalable production of high-purity L-LA and unlocking the full industrial potential of PLA. To address these challenges, we herein explore a diastereomeric crystallization approach that leverages chiral aromatic amines, aiming to combine high enantioselectivity with operational simplicity and scalability.

Diastereomeric crystallization, which employs a chiral resolving agent to convert enantiomers into diastereomeric salts with distinct solubilities, has emerged as a broadly applicable and promising strategy for chiral resolution.[13–16] For instance, Lam *et al.* demonstrated that *N*-methyl-D-glucamine selectively forms crystalline salts with *S*-ibuprofen enantiomer, yielding >95% optically pure product at 85% efficiency, thereby confirming the method's viability for industrial implementation.[17] This strategy has also demonstrated broad applicability in the resolution of chiral carboxylic acids. Rossi *et al.* systematically investigated the diastereomeric salt formation of representative chiral carboxylic acids, including ibuprofen, naproxen, and ketoprofen, with 1-phenylethylamine, providing structural insights into the chiral recognition mechanisms underlying this approach.[18] González-Sabín and co-workers reported efficient resolutions of α-bromoarylacetates and arylpropiolic acids, further extending the applicability of this method to functionalized carboxylic acids.[19] These examples confirm the versatility of this approach for chiral carboxylic acids. Nevertheless, diastereomeric crystallization has been rarely reported for resolving lactic acid enantiomers. This represents a significant yet underutilized opportunity, as the carboxyl group of lactic acid offers an ideal site for salt formation with chiral bases, a crystallization process facilitated by the molecule's low molecular weight and high polarity. Herein, we report the first comprehensive study on the diastereomeric crystallization of lactic acid using chiral aromatic amines. Systematic screening identified (*R*)-1-phenylpropylamine ((*R*)-1-PA) as a highly effective resolving agent. The enantioselectivity was rationalized through a multiscale investigation combining thermal analysis, single-crystal X-ray diffraction (SCXRD), phase equilibrium studies, and molecular simulations. This work elucidates the structure-energy relationships governing chiral recognition and establishes a robust, scalable process for producing high-purity L-LA from low-grade feedstocks.

2 Results and discussion

The stereochemistry and spatial arrangement of functional groups in chiral resolving agents critically influence the recognition of lactic acid enantiomers and the subsequent formation of diastereomeric salts. To identify effective candidates, the enantiomer-resolving performance of a series of aromatic and aliphatic amines (Fig. 1c) in acetonitrile (MeCN) were evaluated. Low-grade lactic acid (L-LA, 80% *ee*) was used as the starting material, which reflects the composition of industrial crude lactic acid and represents the target feedstock for purification in this study. MeCN was chosen for its moderate polarity and good solvation ability, which facilitate selective salt precipitation.[20] Fig. 1d systematically compares the chiral resolution performance of these agents under identical crystallization conditions. It should be emphasized that, because Fig. 1d starts from an L-enriched lactic acid feed rather than a racemic mixture, the observed preferential crystallization cannot be inferred solely from the intrinsic lattice stability of the isolated diastereomeric salts. Instead, the crystallization outcome is determined by the phase-equilibrium path of the multicomponent system under the selected operating conditions, including feed composition, solvent, temperature, and cooling trajectory. The screening results revealed a striking discrepancy in diastereomeric discrimination among various resolving agents: the highest resolution efficiency (≥99% *ee*, 70% yield) was achieved by (*R*)-1-PA, closely followed by (*R*)-1-phenylethylamine ((*R*)-1-PEA) (≥97% *ee*, 68% yield). In stark contrast, the (*S*)-configured counterparts ((*S*)-1-PA or (*S*)-1-PEA) exhibited poor yields (≤30%), a behavior attributable to the "rule of reversal" in chiral resolution,[21,22] whereby these amines are expected to preferentially bind D-lactic acid (D-LA). For the aliphatic amine 1-cyclopropylethylamine (1-CPEA), the enantiomeric configuration significantly influences the resolution performance. Specifically, (*R*)-1-CPEA exhibits better performance than (*S*)-1-CPEA; however, even the former affords only approximately 90% *ee* of L-LA with a crystallization yield of 13%, which is still substantially inferior to those obtained with the aromatic amines (*R*)-1-PA and (*R*)-1-PEA. These results indicate that stereochemical matching alone is insufficient to achieve efficient chiral resolution. The limited performance of aliphatic amines may be attributed to their high conformational flexibility and the absence of aromatic moieties, which collectively hinder the formation of stable diastereomeric salts and effective chiral discrimination.[23] Similarly, although amino alcohols are chiral, their hydroxyl groups are readily solvated in polar solvents, which shields the amine functionality and weakens ion-pair interactions with lactic acid.[24] These results indicate that, in addition to possessing an appropriate configuration, an ideal resolving agent should simultaneously exhibit molecular rigidity, moderate basicity, and aromaticity (Table S1). (*R*)-1-PA exemplifies this design principle: its primary amine forms a strong ionic interaction with L-LA, its aromatic ring provides structural rigidity, and its chiral center adopts a spatial configuration that is complementary to L-LA. To translate these empirical insights into rational design framework, a molecular-level understanding of the chiral recognition mechanism is essential. We therefore conducted detailed structural and energetic analyses of the (*R*)-1-PA system to elucidate the origins of its superior performance.

To elucidate why (*R*)-1-PA and (*R*)-1-PEA exhibit superior performance, we first probed the molecular interactions during salt formation. Fourier-transform infrared (FTIR) spectroscopy was employed to systematically analyze the evolution of characteristic vibrational signatures of key functional groups throughout the crystallization process. As shown in Fig. S1, all samples exhibited a distinct C–O stretching vibration near 1120 cm^{-1}, which remained largely unaltered upon salt formation. Pure D-LA and L-LA displayed a broad absorption band between 3200 cm^{-1} and 3600 cm^{-1}, attributable primarily to adsorbed water and –OH groups. The N–H stretching vibrations of (*R*)-1-PA, observed between 3300 cm^{-1} and 3500 cm^{-1}, disappeared following crystallization, indicating proton transfer during salt formation. Additionally, delocalization of the negative charge on the carboxylate group in the crystalline salt resulted in two new absorption bands: an asymmetric stretching mode at 1550–1650 cm^{-1} and a symmetric stretching mode near 1400 cm^{-1}.[25,26] These spectral changes unequivocally confirm the formation of ionic diastereomeric salts through acid–base neutralization between lactic acid enantiomers and chiral aromatic amines, providing direct evidence of molecular structural reorganization during salt crystallization. Beyond these vibrational signatures, the electrostatic complementarity between lactic acid and the resolving agents provides further insight into the driving force for salt formation. Electrostatic potential (ESP) surface analyses (Fig. 2a and 3a) revealed the molecular electrostatic basis for salt formation. The deprotonated carboxylate region of lactic acid exhibits negative electrostatic potential, whereas the protonated ammonium region of (*R*)-1-PA and (*R*)-1-PEA displays strong positive potential. The resulting spatial complementarity of these electrostatic potential distributions not only facilitates proton transfer but also renders salt formation thermodynamically favorable. Collectively, the appearance and disappearance of key vibrational bands in the FTIR spectra, together with the ESP complementarity, provide a comprehensive validation—from both vibrational spectroscopy and electronic structure perspectives—that ionic diastereomeric salts are formed *via* a well-defined proton transfer mechanism during chiral resolution. These molecular-level proton transfer events and electrostatic interactions not only confirm salt formation but also establish a foundation for understanding the solid-state stability and enantioselectivity of the resulting diastereomeric salts.

Having established the molecular basis for salt formation, we systematically characterized the resulting crystalline structures to elucidate how these intermolecular interactions govern crystal packing and, ultimately, separation performance. By integrating thermal analysis with crystallographic characterization, this study systematically delineates the structure-energy relationships of the resulting diastereomeric crystalline salts. As shown in Fig. S2, four crystals exhibit long needle-like morphologies. The experimental PXRD patterns exhibit excellent agreement with the corresponding simulated diffractograms (Fig. S3), thereby confirming the reliability of the resolved crystal structures. All four salts, (*R*)-1-PA-D (CCDC: 2491484), (*R*)-1-PA-L (CCDC: 2491485), (*R*)-1-PEA-D (CCDC: 2491489) and (*R*)-1-PEA-L (CCDC:

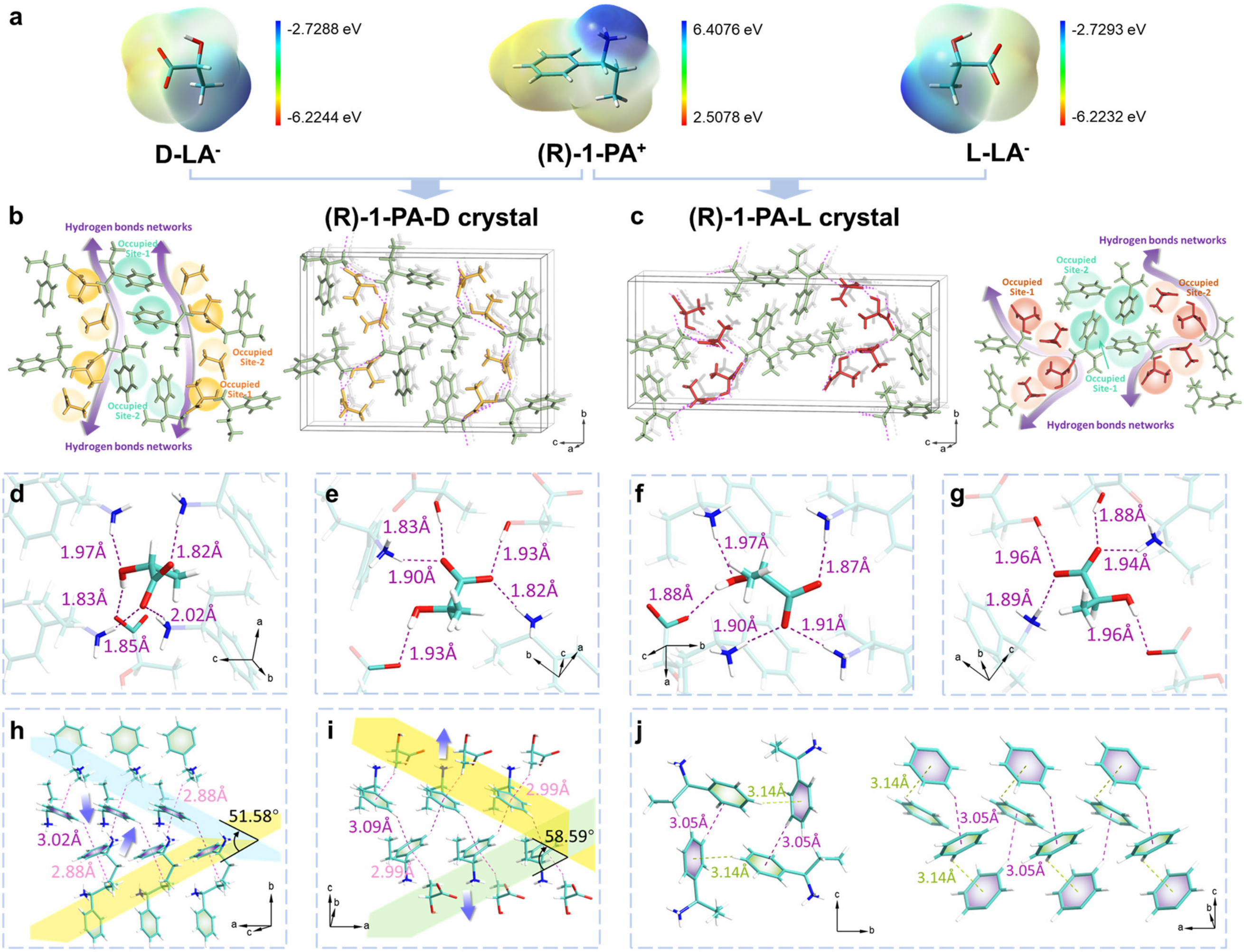

Fig. 2 Molecular electrostatic complementarity and crystalline structures of (*R*)-1-PA diastereomeric salts. (a) The electrostatic potential (ESP) surface map of D-LA$^-$, L-LA$^-$, and (*R*)-1-PA$^+$; crystalline structures and hydrogen-bonding motifs of (b) (*R*)-1-PA-D and (c) (*R*)-1-PA-L, dark yellow and light yellow sphere represent the occupied site-1 and occupied site-2 of D-LA, while dark cyan and light cyan sphere represent the occupied site-1 and occupied site-2 of (*R*)-1-PA; local hydrogen-bond networks for (d) the site-1 D-LA and (e) the site-2 D-LA in (*R*)-1-PA-D, (f) the site-1 L-LA and (g) the site-2 L-LA in (R)-1-PA-L; comparative π–π stacking environments for (h) the site-1 (*R*)-1-PA and (i) the site-2 (*R*)-1-PA in (*R*)-1-PA-D; (j) the helical four-membered stacking motif for (*R*)-1-PA-L. Hydrogen bonds are shown as magenta dashed lines. Color scheme for atoms: C, dark cyan; N, blue; O, red; H, white.

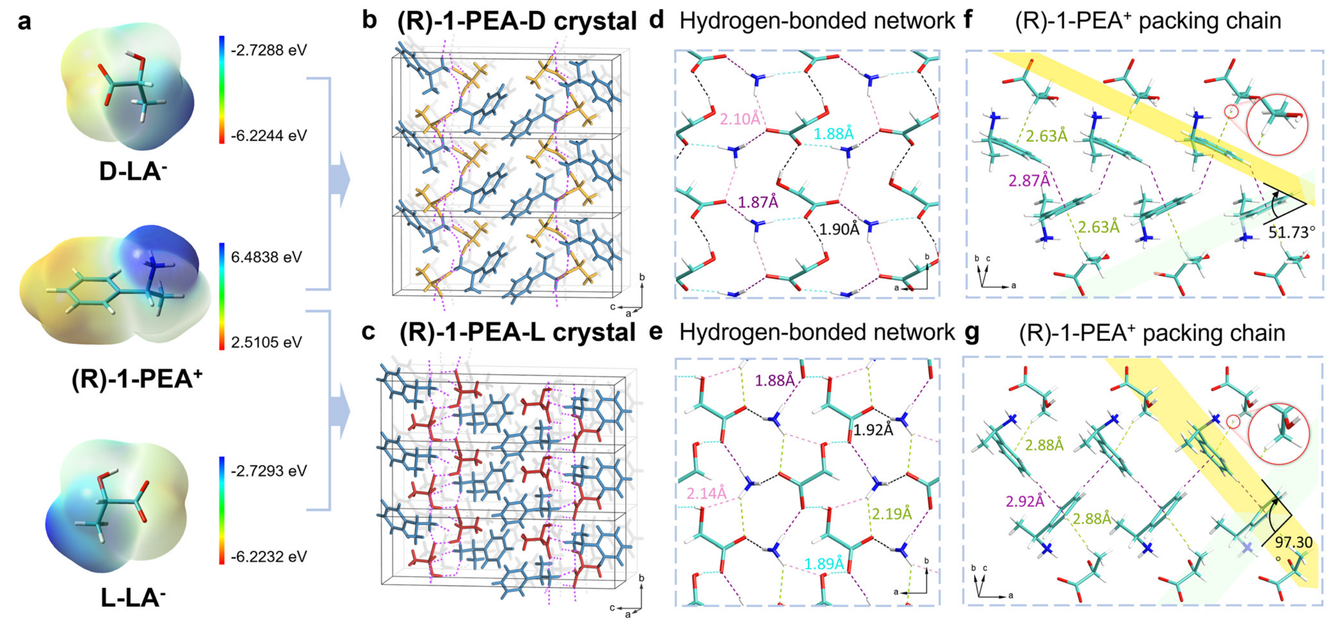

Fig. 3 Molecular electrostatic complementarity and crystalline structures of (*R*)-1-PEA diastereomeric salts. (a) The electrostatic potential (ESP) surface map of D-LA$^-$, L-LA$^-$, and (*R*)-1-PEA$^+$; crystalline structures and hydrogen-bonding motifs of (b) (*R*)-1-PEA-D and (c) (*R*)-1-PEA-L; local hydrogen-bond networks for (d) (*R*)-1-PEA-D and (e) (*R*)-1-PEA-L; comparative π–π stacking environments for (f) (*R*)-1-PEA-D and (g) (*R*)-1-PEA-L; hydrogen bonds are shown as magenta dashed lines. Color scheme for atoms: C, dark cyan; N, blue; O, red; H, white.

2491490), crystallize in the orthorhombic system and belong to the same $P2_12_12_1$ space group (Table S2). They exhibit highly ordered three-dimensional packing networks with no solvent molecules present within the lattice. Despite their identical crystallographic symmetry, the salts display pronounced differences in local packing arrangements, hydrogen-bonding topologies, and π–π stacking geometries. These subtle yet significant structural divergences ultimately govern the thermodynamic stability of the diastereomeric salts and provide the intrinsic driving force for their chiral discrimination throughout the crystallization process. As presented in Fig. 2b and c, the crystal structures of both (*R*)-1-PA-D and (*R*)-1-PA-L contain two crystallographically independent components (designated as site-1 and site-2), reflecting the intrinsic asymmetry within the primitive unit cell. In (*R*)-1-PA-D, the D-LA and (*R*)-1-PA molecules at the two sites are alternately arranged and assemble into distinct molecular chains extending along the *b* axis. These chains are further interconnected through a hydrogen-bonding network-oriented perpendicular to the *c* axis (represented as the purple double-headed arrows), forming a layered architecture propagating along the *a* axis. The D-LA molecules at both sites exhibit highly saturated coordination environments (Fig. 2d and e). At site 1, D-LA participates in multiple N–H⋯O and O–H⋯O interactions with four protonated ammonium (NH_3^+) groups of (*R*)-1-PA and one neighboring D-LA molecule, with hydrogen-bond lengths ranging from 1.82 to 2.02 Å. At site 2, D-LA is anchored by two NH_3^+ groups of (*R*)-1-PA and three adjacent D-LA molecules through a dense hydrogen-bonding network (1.82–1.93 Å), including exceptionally short carboxylic O–H⋯O contacts that markedly enhance electrostatic and directional intermolecular interactions.

In (*R*)-1-PA-L, the L-LA molecules at both sites also adopt an alternating arrangement with (*R*)-1-PA, assembling into more contorted molecular chains extending along the *b* axis (represented by purple double-headed arrows). At site-1, L-LA is anchored through multiple N–H⋯O and O–H⋯O interactions involving four surrounding NH_3^+ groups and one neighboring L-LA molecule, with slightly elongated hydrogen-bond lengths of 1.87–1.97 Å. At site-2, L-LA is stabilized by a hydrogen-bonding network comprising two NH_3^+ groups and three adjacent L-LA molecules (1.88–1.96 Å), reflecting subtle yet significant differences in the local coordination environments (Fig. 2f and g). The π–π stacking between the aromatic amines further highlights the symmetry differences between the two sites (Fig. 2h and i). Paired edge-to-face π–π interactions between (*R*)-1-PA molecules at equivalent orientations result in zigzag chains that propagate along the *a* axis. At site 1, the NH_3^+ groups of (*R*)-1-PA chains point inward (blue arrows), with an interplanar angle of 51.58° and C–H⋯π distances of 3.02 Å, complemented by additional C–H⋯π contacts (2.88 Å) with alkyl chains from (*R*)-1-PA molecules of site 2. At site 2, the NH_3^+ groups of (*R*)-1-PA point outward, and the staggered benzene rings adopt a slightly larger interplanar angle (58.59°); the π-stacking is reinforced by anchoring between the aromatic rings and multiple C–H⋯π interactions involving the methyl groups of D-LA (2.99 Å). In contrast, the L-LA chain in (*R*)-1-PA-L is more contorted due to the alternating arrangement of L-LA molecules across two sites, while the two (*R*)-1-PA molecules at both sites assemble into a helical four-membered stacking motif, with inter-site C–H⋯π contacts of 3.05 Å and 3.14 Å, respectively. The unit cell contracts along the *a* axis and *b* axis directions but elongates substantially along the *c* axis. The shortening of the *a* axis decreases the inter-ring distance of (*R*)-1-PA, whereas the pronounced extension of the c axis renders the overall packing more diffuse. This structural relaxation is accompanied by slightly elongated hydrogen-bond lengths and weakened π–π interaction between (*R*)-1-PA molecules (Fig. 2j). This less efficient packing in (*R*)-1-PA-L directly correlates with lower lattice stability, consistent with its lower lattice energy (286.60 kcal mol^{-1}) and enthalpy of fusion (17.17 kcal mol^{-1}) relative to (*R*)-1-PA-D (332.92 kcal mol^{-1}; 22.84 kJ mol^{-1}) (Fig. S4, Table S3).

In contrast to the crystal structures of the (*R*)-1-PA salts, all components in the crystallographically independent units of (*R*)-1-PEA-D and (R)-1-PEA-L occupy symmetrical-equivalent positions. In each structure, lactic acid and (*R*)-1-PEA assemble into chain-like motifs propagating along the *b* axis, which are further crosslinked by hydrogen-bonded networks oriented perpendicular to the *c* axis, forming a three-dimensional framework (Fig. 3b and c). Despite their identical packing dimensionality, the configurational difference between D-LA and L-LA engenders marked variations in both the number and spatial arrangement of intermolecular hydrogen bonds (Fig. 3d and e). The (*R*)-1-PEA-L salt adopts a more regular and densely connected hydrogen-bond network, leading to stronger cohesive interactions and a correspondingly higher melting point (142.83 °C) (Fig. S4d). Both crystals exhibit edge-to-face π–π stacking. In (*R*)-1-PEA-D, the interplanar angle between the phenyl rings is 51.73°, whereas in (*R*)-1-PEA-L, they approach a nearly orthogonal orientation (97.30°). The nearly orthogonal orientation facilitates offset π–π stacking, a geometry less sensitive to interplanar distances, thereby compensating for the increased centroid separation and resulting in enhanced π–π interactions. The configuration-dependent packing is further manifested in contrasting C–H⋯π interactions: those in (*R*)-1-PEA-D originating from the –CH group of D-LA, and those in (*R*)-1-PEA-L from the $-CH_3$ group of L-LA, thereby amplifying the stereochemical divergence (Fig. 3f and g). These differences are also directly reflected in the solid-state stability and hygroscopic behavior of the materials: (*R*)-1-PEA-D exhibits pronounced hygroscopicity, whereas (*R*)-1-PEA-L displays enhanced stability. Experimental characterization unambiguously confirms that the isolated (*R*)-1-PEA-D solid comprises a mixed phase of the anhydrous form and its monohydrate counterpart (Fig. S3c). The TGA analysis reveals a weight loss of approximately 6.98%, accompanied by a sharp endothermic event in the DSC trace, indicative of crystalline dehydration (Fig. S4c). Calculations based on this weight loss correspond to a monohydrate content of approximately 88.06% and an anhydrous fraction of about 11.94% in the sample. The resulting monohydrate, (*R*)-1-PEA-D·H_2O, features a significantly more compact hydrogen-bond network with shorter bond distances, together with a transformation of the aromatic stacking mode from a parallel to a zigzag arrangement (C–H⋯π = 3.03 Å) (Fig. S5). Evidently, incorporation of water molecules effectively compensates for the stereochemically induced deficiencies in intermolecular interactions of (*R*)-1-PEA-D, concurrently reducing excess lattice voids and promoting a denser, more efficiently packed crystal architecture. This brings into sharper focus the perfect stereochemical complementarity of the anhydrous, stable (*R*)-1-PEA-L salt, fundamentally explaining their different thermal properties from a molecular level. Consistent with PXRD analysis, all diastereomeric salts exhibit identical diffraction patterns under varying crystallization conditions, with no peak shifts or additional reflections, demonstrating their high structural uniformity and thermodynamic stability (Fig. S6).[27,28] Taken together, the combined structural and thermal analyses delineate a coherent structure-energy relationship across the diastereomeric salts, revealing systematic differences in hydrogen-bond network topology, π-stacking geometry, and overall packing density. These structural distinctions are expected to translate into measurable differences in thermodynamic stability, which we next quantified through solubility and phase equilibrium studies.

To quantify this structure–property relationship for rational guidance on crystallization process development, we measured the solubility of all four salts and constructed three-component phase diagrams. The monotonic increase in solubility with temperature for all salts in MeCN demonstrates their characteristic endothermic dissolution behavior (Fig. 4a and b). These solubility patterns closely reflect the underlying structural distinctions. (*R*)-1-PA-L, with a relatively loose hydrogen-bond network and weaker π–π stacking (indicated by its lower lattice energy), displays significantly higher solubility across the entire temperature range compared to the more densely packed (*R*)-1-PA-D. By contrast, the (*R*)-1-PEA salts, characterized by strong directional hydrogen bonds and nearly orthogonal phenyl ring stacking, adopt more compact crystal lattices, resulting in lower overall solubility than the (*R*)-1-PA series. Notably, the elevated melting point of (*R*)-1-PEA-L (142.8 °C) corresponds to its higher lattice energy. Although the solubility profiles of the (*R*)-1-PA-D/L-LA and (*R*)-1-PEA-D/L-LA salts show opposite trends, both systems achieve comparable resolution efficiencies. Selective crystallization is primarily governed by the relative supersaturation of the target L-LA diastereomeric salt with respect to its enantiomer, rather than by the absolute solubility value. In (*R*)-1-PA system, the L-enriched initial composition ensures that the target salt reaches supersaturation first, leading to preferential crystallization and effective chiral resolution. Thus, the differences in solubility profiles do not contradict the similar resolution performance observed experimentally. These findings indicate that subtle variations in noncovalent interactions at the molecular scale directly translate into measurable differences in macroscopic solubility, providing a clear structure–property relationship that underpins the thermodynamic driving forces for enantioselective crystallization. Based on the observed solubility differences, we constructed isothermal ternary phase diagrams of the MeCN/(*R*)-1-PA-D/(*R*)-1-PA-L system at 30–40 °C (Fig. 4c and d). The three vertices of the diagrams correspond to pure (*R*)-1-PA-D (A), pure (*R*)-1-PA-L (B), and pure MeCN (C), respectively, allowing clear delineation of the single-phase, two-phase, and three-phase eutectic regions. With increasing temperature, the single-

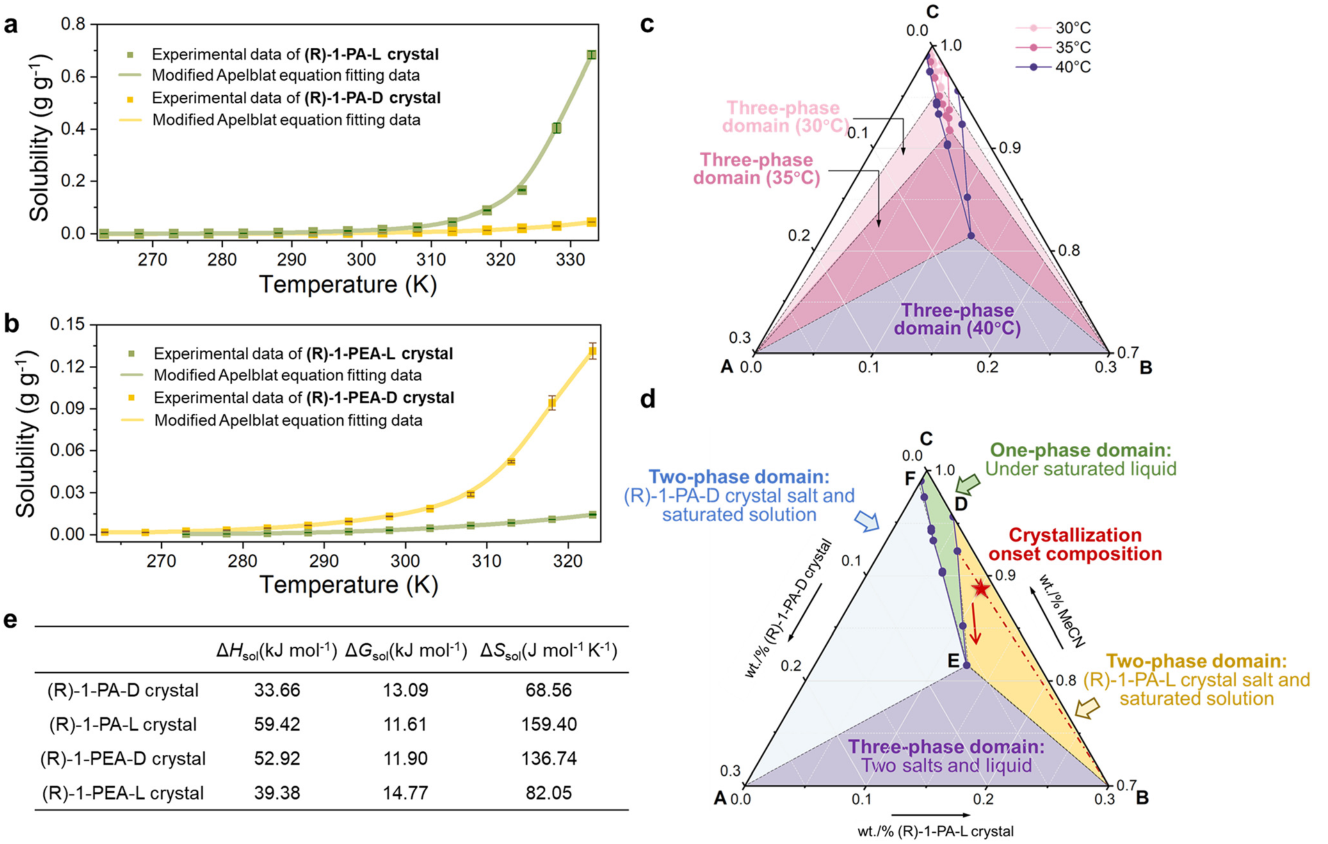

	ΔH_{sol}(kJ mol^{-1})	ΔG_{sol}(kJ mol^{-1})	ΔS_{sol}(J mol^{-1} K^{-1})
(R)-1-PA-D crystal	33.66	13.09	68.56
(R)-1-PA-L crystal	59.42	11.61	159.40
(R)-1-PEA-D crystal	52.92	11.90	136.74
(R)-1-PEA-L crystal	39.38	14.77	82.05

Fig. 4 Thermodynamic basis for diastereomeric crystallization. Solubility profiles of (a) (*R*)-1-PA-D and (*R*)-1-PA-L diastereomeric salts in MeCN, and (b) (*R*)-1-PEA-D and (*R*)-1-PEA-L diastereomeric salts in MeCN; (c) schematic illustration of the ternary phase diagrams of the (*R*)-1-PA-D system at different temperatures; (d) schematic illustration of the ternary phase diagram at 40 °C for (*R*)-1-PA-D system, showing the crystallization domains, the slopes of the fitted solubility curves, and the migration path of the crystallization point; (e) dissolution thermodynamic parameters for diastereomeric crystal.

phase region expands, while the two-phase region, in which the solution coexists with solid salts, shifts toward higher total solute compositions, in agreement with the observed increase in solubility. Analysis of the ternary phase diagram at 40 °C shows that the initial composition (red pentagram) resides within the crystallization domain of the L-type diastereomeric salt ((R)-1-PA-L) and lies precisely on the liquid–solid equilibrium tie-line connecting the pure (*R*)-1-PA-L solid vertex with its corresponding saturated solution (red dot-dash line). This indicates that at 40 °C, the selected composition is in equilibrium with the (*R*)-1-PA-L solid phase, thereby thermodynamically predisposing the system toward preferential crystallization of the L-type salt during cooling. Therefore, in the present L-enriched system, the preferential crystallization of (*R*)-1-PA-L does not imply that this salt is intrinsically more stable than (*R*)-1-PA-D. On the contrary, although (*R*)-1-PA-L is the thermodynamically less stable and more soluble isolated salt, the chosen overall composition and cooling path render it the only selectively supersaturated phase, while nucleation of (*R*)-1-PA-D remains thermodynamically disfavored under these conditions. Thermodynamic parameters (Fig. 4e) further corroborate this preference: the dissolution enthalpy of (*R*)-1-PA-L (ΔH_{sol} = 59.42 kJ mol^{-1}) is substantially higher than that of (*R*)-1-PA-D (33.66 kJ mol^{-1}), indicating stronger temperature dependence of its solubility.

Consequently, cooling generates a larger supersaturation driving force for (*R*)-1-PA-L. As the temperature decreases, the liquid-phase composition migrates along the (*R*)-1-PA-L solubility curve toward the eutectic point (E), following the red-arrow trajectory, while the system's state evolves along the tie-lines. The fixed overall composition point moves progressively closer to the solid vertex on the tie-line, as dictated by the lever rule. This evolution pathway ensures that the system remains supersaturated exclusively with respect to the L-type salt while staying well outside the nucleation zone of (*R*)-1-PA-D. From a thermodynamic perspective, such persistent spatial separation within the composition space effectively suppresses nucleation of (*R*)-1-PA-D, thereby enabling highly selective crystallization of (*R*)-1-PA-L. The constructed phase diagram reveals that lower temperatures enlarge the biphasic crystallization region and increase supersaturation, thereby promoting higher yields, whereas higher temperatures expand the single-phase domain, facilitating complete dissolution and efficient mixing. Collectively, by judiciously selecting the initial composition and crystallization temperature, the ternary phase diagrams provide a robust framework for directed and efficient separation of the target diastereomeric salt. To further quantify the coupling between solubility behavior and structural features, the binary solubility data were fitted using thermodynamic models. The modified Apelblat equation provided excellent agreement with the temperature-dependent solubility profiles for all systems (Table S4). Thermodynamic parameters derived from the fitting (Fig. 4e) indicate that the dissolution of all lactic acid salts is endothermic ($\Delta H_{\mathrm{sol}} > 0$) and associated with a positive standard dissolution Gibbs free energy change ($\Delta G_{\mathrm{sol}} > 0$), indicating a non-spontaneous process under standard conditions. The positive ΔG_{sol} is predominantly governed by the unfavorable enthalpy change, while the positive entropy change ($\Delta S_{\mathrm{sol}} > 0$) contributes favorably but is insufficient to overcome the enthalpic barrier, resulting in an overall non-spontaneous dissolution process. Furthermore, ternary phase diagram data were fitted using activity coefficient models to account for non-ideal interactions among multiple components, yielding the corresponding parameters (a_{ij}, b_{ij}) and fitting statistics, as summarized in Table S5. The Wilson model yielded a root-mean-square angular deviation (RAD) of 8.80% and a root-mean-square deviation (RMSD) of 0.69%, whereas the non-random two-liquid (NRTL) model gave a slightly higher RAD (14.09%) and a comparable RMSD (0.61%), indicating that both models achieve high fitting accuracy and satisfactory thermodynamic consistency. The simulated ternary diagrams are in excellent agreement with experimental data (Fig. S7 and S15), confirming the reliability of the models and consolidating a coherent thermodynamic link from molecular structure to

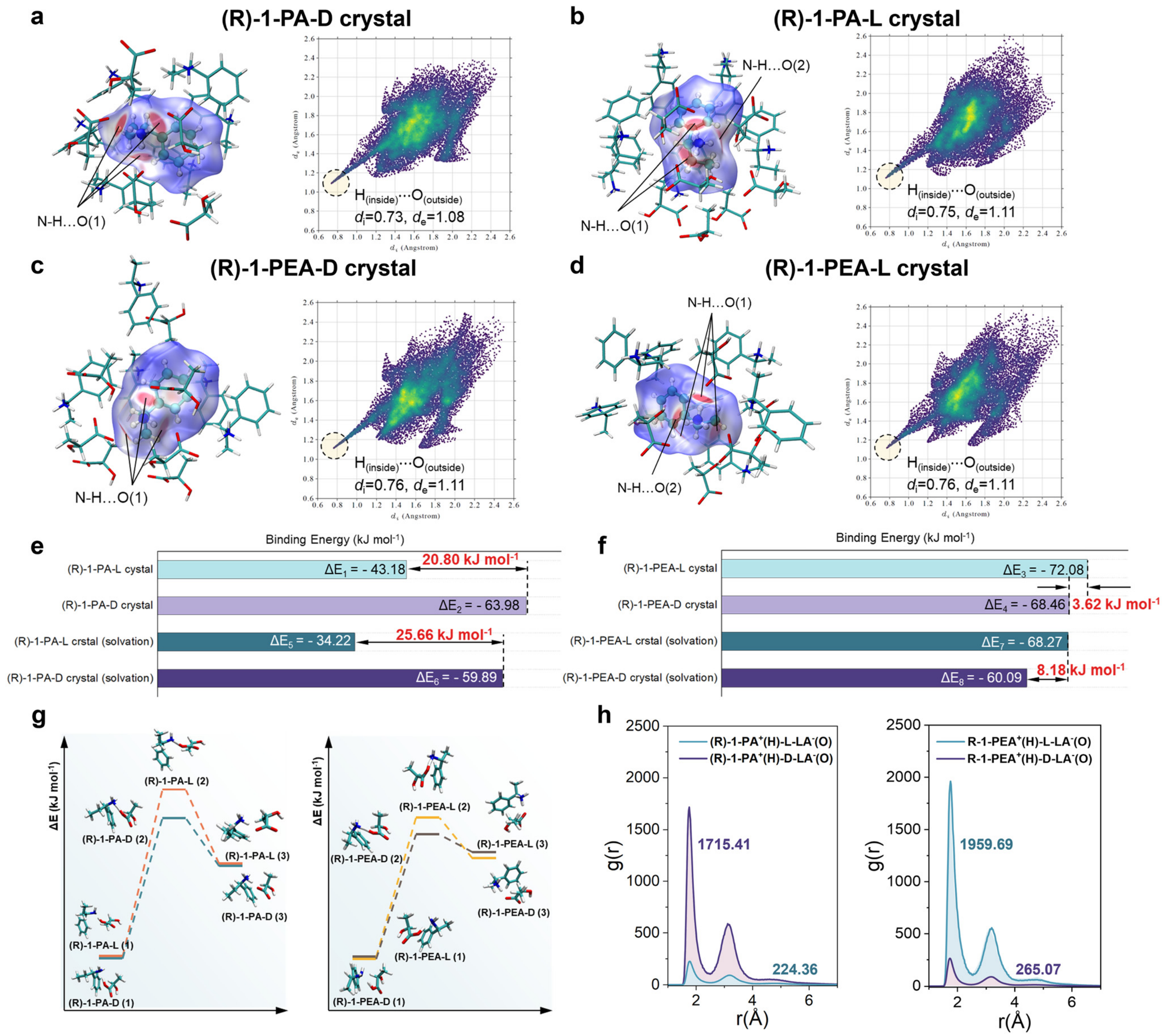

Fig. 5 Molecular simulation results of four crystalline salts. (a–d) Hirshfeld surfaces and 2D fingerprint plots; (e and f) intermolecular binding energies of crystalline salts under solvent and solvent-free conditions; (g) proton transfer energy profile of lactic acid with a chiral resolving agent in MeCN; (h) radial distribution functions (RDFs) of intermolecular interactions in saturated solutions. Color scheme for atoms: C, dark cyan; N, blue; O, red, and H, white.

phase behavior. Collectively, these analyses establish a comprehensive thermodynamic framework encompassing hydrogen-bond network topology, π–π stacking geometry, thermal analysis, and phase equilibrium behavior. The insights provide a predictive mechanistic basis for the selective crystallization of L-LA and lay a tunable thermodynamic foundation for process scale-up. Detailed phase equilibrium data fitting is provided in SI S1.

Hirshfeld surface analysis, combined with 2D fingerprint plots, provides a direct connection between the observed macroscopic thermodynamic trends and the underlying molecular interaction patterns. These macroscopic solubility and phase behavior trends are intrinsically rooted in the underlying non-covalent interaction patterns, which can be further visualized and quantified through Hirshfeld surface analysis and two-dimensional fingerprint plots.[29] Detailed quantitative data is provided in SI S2. As shown in Fig. 5a–d, the interaction patterns revealed by Hirshfeld surfaces and fingerprint plots are in excellent agreement with the hydrogen-bond network topologies, π–π stacking geometries, and local packing motifs determined from SCXRD analysis. Specifically, in the (*R*)-1-PA system, prominent red regions on the Hirshfeld surfaces correspond to the short, highly directional O–H⋯O and N–H⋯O interactions observed crystallographically. These sites engage in multiple N–H⋯O and O–H⋯O contacts at sites 2, with bond lengths concentrated between 1.82–1.93 Å, which underlies the denser hydrogen-bond network and cooperative π–π stacking observed in (*R*)-1-PA-D.[30,31] Consistently, the fraction of H⋯O contacts in (*R*)-1-PA-L (15.23%) is slightly higher than in (*R*)-1-PA-D (13.24%, Fig. S8–S11), yet the former exhibits longer average hydrogen-bond lengths and a more loosely packed unit cell. This comparison indicates a subtle trade-off between the number of hydrogen-bonding interactions (contact fraction) and their strength (bond length), whereby minor geometric variations can be amplified to give rise to pronounced thermodynamic effects. In the (*R*)-1-PEA system, Hirshfeld surface analysis shows that (*R*)-1-PEA-L exhibits the highest proportion of H⋯O contacts (21.61%), consistent with its more compact unit cell and more symmetric molecular arrangement. This finding rationalizes the stronger directional hydrogen-bonding contribution in this polymorph, which, in concert with the π–π stacking geometry, accounts for its enhanced lattice rigidity and elevated thermal stability. Collectively, these distinct intermolecular interaction patterns underline the origin of the efficient separation of L-LA over D-LA.

To quantitatively assess the enantiomeric discrimination imparted by the aforementioned interaction patterns, we calculated the binding energy differences ($|\Delta E_i – \Delta E_j|$) under both solvent-free and implicit solvation (MeCN, SMD model) conditions (Fig. 5e and f, S12 and S13). This energy difference serves as a direct measure of the strength of chiral recognition.[32] In the absence of solvent, the binding energy difference in the (*R*)-1-PA system ($|\Delta E_1 – \Delta E_2|$ = 20.80 kJ mol^{-1}) is markedly larger than that of (*R*)-1-PEA ($|\Delta E_3 – \Delta E_4|$ = 3.62 kJ mol^{-1}), indicating a stronger preference for selective ion-pair formation in the solid state for (*R*)-1-PA. Inclusion of MeCN further increases the binding energy differences to 25.67 kJ mol^{-1} for (*R*)-1-PA ($|\Delta E_5 – \Delta E_6|$) and 8.18 kJ mol^{-1} for (*R*)-1-PEA ($|\Delta E_7 – \Delta E_8|$), highlighting the role of the solvent's polar/dielectric environment in enhancing stereoselectivity. Accordingly, transition state theory (TST) was further employed to elucidate the proton-transfer mechanism, providing molecular-level insights into the solvent-mediated formation of ion-pair complexes. Under solvent-free conditions, the proton-transfer energy profile from the carboxyl oxygen of lactic acid to the chiral amine nitrogen exhibits a mono-tonically increasing trend without a discernible barrier (Fig. S14). In contrast, in the presence of MeCN, a well-defined transition state is observed, indicating that the lactic acid proton can be effectively captured by the resolving agent and form a stable ion-pair complex *via* this transition state (Fig. 5g). These results reveal that solvent-induced polarization redistributes electron density between reactants, substantially lowering the proton-transfer barrier and facilitating proton migration to the nitrogen atom. Overall, MeCN not only accelerates proton transfer but also stabilizes the resulting ion-pair structures through solvation effects, playing a critical role in modulating the formation and stability of diastereomeric salts. To further quantify the specific interactions between the chiral resolving agents and lactic acid in solvent, radial distribution functions (RDFs) between hydrogen atoms of the chiral aromatic amines and oxygen atoms of LA were calculated (Fig. 5h). Although the peak positions are comparable across the systems, notable differences in peak intensities are observed, reflecting distinct local interaction patterns between the resolving agents, D-LA, and L-LA. The RDF peak area of (*R*)-1-PA-D is significantly larger than that of (*R*)-1-PA-L, indicating stronger spatial affinity between D-LA$^-$ and (*R*)-1-PA$^+$ within specific radial distances, in excellent agreement with the previously discussed binding energy and thermodynamic analyses. In contrast, (*R*)-1-PEA exhibits sharper RDF peaks, revealing tighter local interactions between the (*R*)-1-PEA$^+$ and L-LA$^-$. This enhanced local affinity highlights subtle differences in intermolecular interactions, providing a plausible molecular-level driving force for selective aggregation during the crystallization process. Molecular simulations further indicate that the driving force for enantioselective separation of lactic acid does not originate from a single interaction but rather emerges from the cooperative interplay of multiple non-covalent interactions, including directional hydrogen bonding, π–π stacking, and solvation effects, collectively governing both crystallization selectivity and lattice stability.[33] Guided by these molecular insights, we proceeded to design and validate an integrated crystallization process for high-purity L-LA production.

Building upon the aforementioned multiscale understanding, spanning from molecular-level interactions to macroscopic phase behavior, a predictive framework for process design was established. This framework integrated the diastereomeric crystallization strategy into a material-recycling process for producing high-purity L-LA. Based on this approach, we report, for the first time, an integrated process for the highly

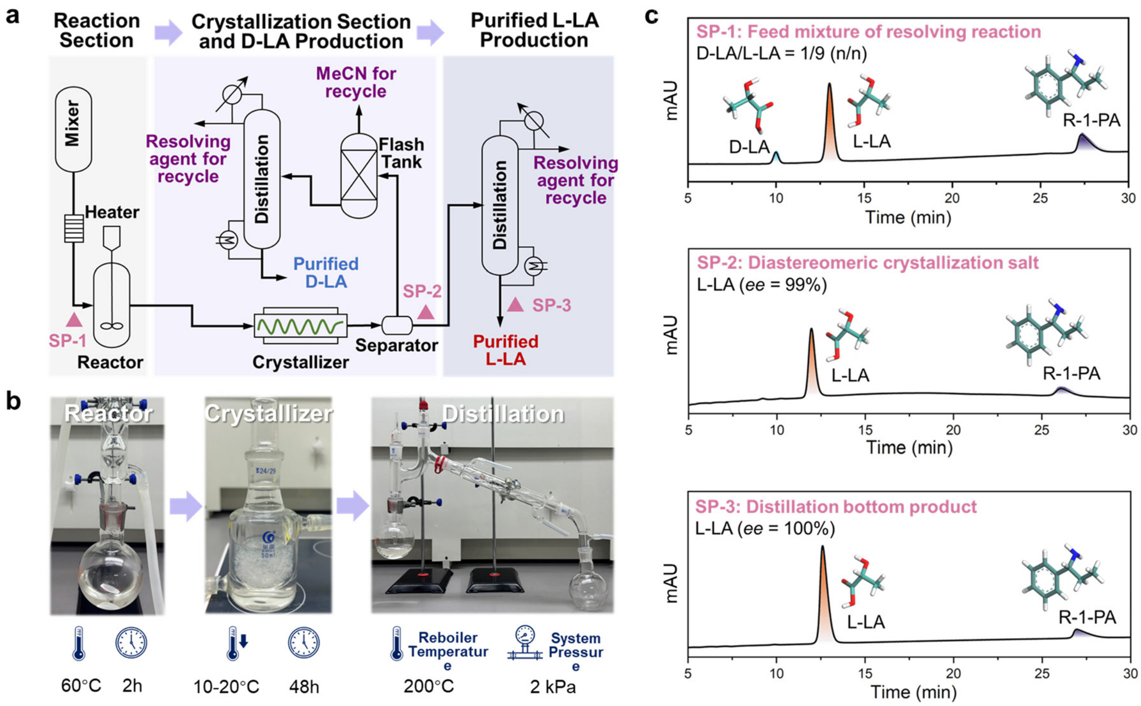

Fig. 6 Integrated process for the production of highly enantiopure L-LA *via* diastereomeric crystallization combined with distillation, with corresponding liquid-phase composition profiles. (a) Schematic representation of the L-LA production process, SP-1, SP-2 and SP-3 denote the sampling points for specific unit operations; (b) laboratory-scale experimental process and parameter setting; (c) high performance liquid chromatography results of different sample points. The *y*-axis represents milli-absorbance units (mAU), where "m" refers to milli (10^{-3}) and "AU" refers to absorbance units.

efficient resolution of lactic acid enantiomers *via* diastereomeric salt formation using chiral aromatic amines as resolving agents. As illustrated in Fig. 6a, the process was successfully implemented at the laboratory scale, integrating reaction, crystallization, separation, and recovery of both solvent and resolving agent. Industrial-grade crude lactic acid (L-LA : D-LA = 9 : 1, mol mol^{-1}; SP-1 in Fig. 6a and c) was reacted with the chiral resolving agent in a stoichiometric ratio at 60 °C under ambient pressure to form a homogeneous solution. The solution was then transferred to a preheated crystallizer and gradually cooled from 60 °C to 10–20 °C, followed by 48 h of aging to promote the selective crystallization of L-enantiomer-enriched diastereomeric salts (Fig. 6b). Solid–liquid separation yielded crystalline salts, which were analyzed by high-performance liquid chromatography (HPLC) to confirm an *ee* of L-LA ≥ 99% (SP-2, Fig. 6a and c). The isolated salt was then subjected to vacuum distillation (reboiler temperature 200 °C, system pressure 2 kPa) to recover L-LA as the bottom product (SP-3, Fig. 6a and c). Detailed material balance information is provided in Table S7 of the SI. Meanwhile, the mother liquor, in which the D-LA molar fraction was increased relative to the initial feed composition (Fig. S16). In principle, solvent recovery can be achieved *via* flash evaporation of MeCN, followed by further distillation to obtain a D-LA-enriched lactic acid mixture, thereby enabling closed-loop recycling of both solvent and resolving agent. About residual resolving agents, efficient removal can be accomplished through multistage rectification combined with optimization of the reflux ratio and operating pressure. Future work will further focus on crystallization process optimization, solvent recovery, green solvent substitution, and the development of more energy-efficient separation strategies from a process optimization perspective, with the aim of improving both economic feasibility and sustainability. Collectively, this process combines selective crystallization with distillation to markedly enhance the enantiomeric purity of lactic acid, increasing the *ee* of L-LA from 80% in the crude feed to ≥99% in the bottom product, and, owing to its comprehensive material-recycling design, demonstrates significant advantages in terms of atom economy, process sustainability, and industrial applicability.

3 Conclusions

In this work, we reported, for the first time, a highly efficient diastereomeric crystallization strategy for the resolution of L-LA from its enantiomer D-LA, employing chiral aromatic amines (*R*)-1-PA and (*R*)-1-PEA as resolving agents. Through integrated multiscale characterization and molecular simulations, we elucidated the formation and structural organization of the diastereomeric salts, revealing a synergistic recognition mechanism driven by electrostatic complementarity, directional hydrogen bonding, and π–π stacking between the chiral amines and lactic acid enantiomers. These insights explicitly demonstrate the critical role of molecular rigidity, aromaticity, and stereochemical complementarity in the rational design of resolving agents. Furthermore, we developed an integrated "reaction-crystallization-distillation" process that enables the laboratory-scale production of L-LA with *ee* ≥ 99% under robust and reproducible conditions. This process is distinguished by a comprehensive material-recycling design that achieves closed-loop recovery of both the solvent (MeCN) and the chiral resolving agents, thereby enhancing atom economy and process sustainability. The crystallization step, strategically guided by quantitative structure-thermodynamics correlations derived from our molecular-level understanding, demonstrates how predictive frameworks established at the molecular scale can be translated into practical process designs. This study presents a highly efficient and scalable strategy for the purification of L-LA with exceptional *ee*, enabling process design and optimization guided by the intrinsic mechanisms of molecular recognition. Beyond lactic acid, the strategic and methodological principles presented here are broadly applicable to the resolution of other chiral acids and biomolecules, providing a paradigm for the rational design, sustainable production and efficient purification of enantiopure compounds across multiple chemical domains.

4 Experimental and calculation section

All chemicals used in this study were of analytical grade or higher and were used as received without further purification unless otherwise stated. Detailed information on the chemical reagents, including their sources and purity, is summarized in Table S1. The crystallization experiments were performed *via* a two-step process comprising *in situ* salt formation followed by cooling crystallization. The L/D-LA (molar ratio 9 : 1) mixture and the corresponding chiral aromatic amine resolving agent were dissolved in 50 mL of MeCN and stirred thoroughly to ensure complete proton transfer and salt formation. The resulting solution was transferred into a jacketed crystallizer and stirred at 60 °C for 1 h to allow for equilibrium and stabilization. Subsequently, the solution was cooled from 60 °C to 10–20 °C using an external refrigeration/heating circulator (Julabo CORIO™ CD-200F, Germany). During cooling, the solution was continuously stirred using a magnetic stirrer (IKA RCT digital, Germany) at a constant rate of 100 rpm. The solution was maintained under static conditions for 48 h to promote crystal growth and enhance the enantiomeric purity of the solid L-LA phase. The resulting solid was collected by vacuum filtration, washed with pre-cooled MeCN to remove residual mother liquor, and dried under reduced pressure, yielding diastereomeric salts with L-LA *ee* ≥ 99% (corresponding to the SP-1 crystallization and separation step in Fig. 6a). The crystallized salt (7 g) was subsequently subjected to dissolution and conversion treatment (corresponding to SP-2 in Fig. 6a), followed by vacuum distillation in a round-bottom flask. Distillation was performed at a system pressure of 2 kPa and a reboiler temperature of 200 °C, affording L-LA of ≥99% enantiomeric purity in the distillation bottom fraction (corresponding to SP-3 in Fig. 6a). The resolving agent ((*R*)-1-PA) can be recovered from the distillation head fraction and recycled, with an overall recovery of approximately 65% in the present crystallization–distillation process. To obtain high-quality single crystals suitable for SCXRD analysis, four diastereomeric salts were prepared using a combination of low-temperature incubation and gradual solvent evaporation. Crystals of (*R*)-1-PA-D/L and (*R*)-1-PEA-D/L were dissolved in MeCN to prepare saturated solutions, which were then filtered through a 0.22 μm membrane and transferred into clean sample vials. The vials were then placed in a refrigerator maintained at 2–4 °C. Colorless, transparent needle-shaped single crystals suitable for SCXRD were obtained after approximately 1–5 days through the combined effects of low-temperature incubation and solvent evaporation. The *ee* of all samples collected during the process was determined *via* HPLC analysis. Measurements were performed on an Agilent 1260 system equipped with a 150 × 4.6 mm Astec® CLC-L chiral column (5 μm particle size, MilliporeSigma). The mobile phase consisted of 0.5 mmol L^{-1} aqueous $CuSO_4$ (pH 4.0), delivered at a flow rate of 1.0 mL min^{-1}. UV detection was set at 254 nm, and the column temperature was maintained at 30 °C. Each sample was analyzed in triplicate, and the relative deviation was kept below 5%.

The solid-state structures, thermal behavior, and key intermolecular interactions of the four diastereomeric salts were systematically investigated using SCXRD, PXRD, FTIR, and TGA-DSC, providing mechanistic insights into their crystallization behavior and resolution efficiency. FTIR was employed to probe functional group vibrations of D/L-LA, chiral resolving agents, and the corresponding diastereomeric salts. Spectra were recorded at room temperature on a Nicolet iS50 FT-IR spectrometer (Thermo Fisher Scientific) equipped with an *in situ* reaction chamber. Solid samples (1–2 mg) were finely ground with spectroscopic-grade KBr (100–200 mg, ≤ 2 μm) and pressed into transparent pellets (10–15 MPa, 1–2 min), with pure KBr used as background. Liquid samples (1–2 drops) were cast as thin films on matched salt windows. Spectra were collected over 500–4000 cm^{-1} at 4 cm^{-1} resolution and averaged over 32 scans. PXRD patterns of the diastereomeric salts were recorded on a SmartLab SE diffractometer (Rigaku, Japan) using Cu Kα radiation (λ = 1.5418 Å) at 40 kV and 40 mA. Prior to measurement, samples were finely ground, sieved, and evenly spread on the sample holder to ensure a flat surface. Data were collected over 2θ = 5–60° at a scan rate of 10° min^{-1}. SCXRD data were collected on an XtaLAB PRO II diffractometer equipped with a micro-focus Cu Kα source (λ = 1.54184 Å, 50 kV, 1 mA) and a HyPix Bantam detector at 150 K. Data reduction was performed using CrysAlisPro, structures were solved by intrinsic phasing with SHELXT in Olex2 and refined against F^2 by full-matrix least-squares using SHELXL. Thermal properties were characterized by TGA-DSC on a simultaneous thermal analyzer (Mettler-Toledo, Shanghai, China) under a nitrogen purge (50 mL min^{-1}). Approximately 5.0 ± 0.1 mg of sample was placed in an alumina crucible and heated at 10 °C min^{-1}. DSC thermograms were processed using STARe software, and fusion enthalpies (ΔH_{fus}) were determined by peak integration of the endothermic melting transitions.

To evaluate the thermodynamic behavior of the crystallization process, the solubilities of four crystalline salts in MeCN were determined using the static gravimetric method.[34] In each experiment, excess solid salt was added to preheated MeCN in a sealed, jacketed vessel, and the temperature was maintained within ±0.5 °C using a thermostatic water bath (Julabo CORIO™ CD-200F, Germany). The suspension was stirred continuously for 24 h, with a minimum equilibration period of 6 h. After equilibration, the saturated solutions were filtered through preheated 0.22 μm syringe filters prior to solute content analysis. All measurements were performed in triplicate, and solubility was expressed as the mass ratio of solute to solvent (g g^{-1}). Simultaneously, to delineate the optimal crystallization domain, ternary phase diagrams of the diastereomeric salts formed between the most effective resolving agent, (*R*)-1-PA, and D/L-LA in MeCN were constructed. Solid–liquid equilibrium data for mixtures of varying compositions were determined at different temperatures using the same static gravimetric approach.[35] The resulting solubility data and ternary phase diagrams provide critical guidance for the design of enantioselective crystallization protocols and offer a theoretical basis for optimizing experimental conditions to enhance crystallization selectivity and yield.

In this work, the Molclus program developed by Lu *et al.*[36] was combined with MOPAC[37] and Gaussian16 (ref. 38) to investigate the relative energies of different conformers formed between chiral resolving agents and D/L-LA, with the aim of identifying the most stable structures. Initial conformational pre-optimization was performed using MOPAC at the PM6-DH+ level, followed by full geometry optimization and energy evaluation using Gaussian 16 at the B3LYP/6-311+G(2d,p) level with D3 (BJ) dispersion correction.[39] The preferential intermolecular binding sites were elucidated by projecting the electrostatic potential (ESP) onto the Bader-defined van der Waals surface ($\rho = 0.001$ e Bohr^{-3}), a representation that captures the essential electron–density envelope and molecular shape. The proton transfer reaction between lactic acid and the resolving agent in solution was analyzed using transition state theory (TST). Each identified transition state exhibited a single imaginary frequency, which was further validated through intrinsic reaction coordinate (IRC) calculations to confirm that the corresponding vibrational mode connects the reactant and product along the reaction pathway. The SMD implicit solvation model was employed to evaluate the solvent effect on the interactions between the resolving agents and D/L-LA. The wave function analysis program Multiwfn 3.8 developed by Lu *et al.*[40] was used to investigate the interaction between different chiral resolving agents and D/L-LA. Hirshfeld surface analysis and 2D fingerprinting were used to explore the interactions between the central molecule ((*R*)-1-PA or (*R*)-1-PEA) and surrounding molecules in the crystal lattice, and to analyze the contributions of different atomic forces.[41] GROMACS 2022 was used to investigate the dynamic behavior of salt formation between different chiral resolving agents and D/L-LA.[42] The topology and .gro files of the molecules required for MD were generated by the Sobtob program.[43] Multiwfn 3.8 was used to calculate standard RESP charges, and the GAFF force field was applied to parameterize the molecules. The composition of each simulation box is provided in Table S6. Periodic boundary conditions were applied to eliminate boundary artifacts. To minimize kinetic limitations associated with low temperatures, 333.15 K was selected as the simulation temperature. After minimizing energy, the system temperature was first raised from 0 K to 298.15 K using a V-rescale thermostat in the NVT ensemble. Subsequently, V-rescale and Berendsen were used in the NPT ensemble to stabilize the system at 333.15 K and 1 bar. Finally, a 50 ns production run was performed using the V-rescale thermostat and the Parrinello–Rahman barostat to ensure sufficient equilibration. Radial distribution functions (RDFs) were calculated from the equilibrated trajectories to quantitatively assess intermolecular interactions and spatial correlations between components.

Author contributions

Yuanyuan Shen: conceptualization, data curation, formal analysis, investigation, methodology, validation, software, visualization, writing – original draft. Ying Liu: supervision, visualization, project administration, conceptualization, writing – review & editing. Zexiang Ding: software. Jiaqi Li: methodology. Rundao Chen: formal analysis. Feng Zhou: resources. Lihang Chen: software. Qimei Sun: resources. Yuli Bai: writing – review & editing. Zhiguo Zhang: funding acquisition, resources, writing – review & editing. Qiwei Yang: funding acquisition, resources, writing – review & editing. Kai Qiao: resources. Qilong Ren: funding acquisition, resources, writing – review & editing. Zongbi Bao: funding acquisition, project administration, supervision, conceptualization, resources, writing – review & editing.

Conflicts of interest

The authors declare no conflict of interest.

Data availability

Data for this work is provided in the supplementary information (SI) and any additional or raw data is available upon reasonable request from authors.

Supplementary information is available. See DOI: https://doi.org/10.1039/d6im00074f.

CCDC 2491484, 2491485 and 2491489–2491491 contain the supplementary crystallographic data for this paper.[44a–e]

Acknowledgements

This work was supported by the National Natural Science Foundation of China (No. 22225802, No. 22421004, No. 22288102, No. 22208288) and Zhejiang Provincial Natural Science Foundation of China (No. LZ26B060004).

References

1 C. Hu, Y. Zhang, X. Pang and X. Chen, Poly (lactic acid): Recent stereochemical advances and new materials engineering, *Adv. Mater.*, 2025, **37**, 2412185.

2 C. L. Zaccaria, V. Cedrati, A. Nitti, E. Chiesa, A. M. de Ilarduya, M. Garcia-Alvarez, M. Meli, G. Colombo and D. Pasini, Biocompatible graft copolymers from bacterial poly (γ-glutamic acid) and poly (lactic acid), *Polym. Chem.*, 2021, **12**, 3784–3793.

3 K. Stefaniak and A. Masek, Poly (lactic acid) (PLA)-Short review of synthesis methods, properties, recent progress, and new challenges, *eXPRESS Polym. Lett.*, 2025, **19**, p386.

4 A. Mehmood, N. Raina, V. Phakeenuya, B. Wonganu and K. Cheenkachorn, The current status and market trend of polylactic acid as biopolymer: Awareness and needs for sustainable development, *Mater. Today*, 2023, **72**, 3049–3055.

5 K. M. Nampoothiri, N. R. Nair and R. P. John, An overview of the recent developments in polylactide (PLA) research, *Bioresour. Technol.*, 2010, **101**, 8493–8501.

6 Z. Q. Wan, J. M. Longo, L. X. Liang, H. Y. Chen, G. J. Hou, S. Yang and X. B. Lu, Comprehensive understanding of polyester stereocomplexation, *J. Am. Chem. Soc.*, 2019, **141**, 14780–14787.

7 B. H. Tan, J. K. Muiruri, Z. Li and C. He, Recent progress in using stereocomplexation for enhancement of thermal and mechanical property of polylactide, *ACS Sustainable Chem. Eng.*, 2016, **4**, 5370–5391.

8 J. O. C. de França, D. da Silva Valadares, M. F. Paiva, S. C. L. Dias and J. A. Dias, Polymers based on PLA from synthesis using D, L-lactic acid (or racemic lactide) and some biomedical applications: A short review, *Polymers*, 2022, **14**, 2317.

9 X. Ye, J. Cui, B. Li, N. Li, R. Wang, Z. Yan and X. Wan, Enantiomer-selective magnetization of conglomerates for quantitative chiral separation, *Nat. Commun.*, 2019, **10**, 1964.

10 H. Lorenz and A. Seidel-Morgenstern, Processes to separate enantiomers, *Angew. Chem., Int. Ed.*, 2014, **53**, 1218–1250.

11 P. Hadik, L. P. Szabó, E. Nagy and Z. Farkas, Enantioseparation of D, L-lactic acid by membrane techniques, *J. Membr. Sci.*, 2005, **251**, 223–232.

12 C. Gao, X. Xu, C. Hu, W. Zhang, Y. Zhang, C. Ma and P. Xu, Pyruvate producing biocatalyst with constitutive NAD-independent lactate dehydrogenases, *Process Biochem.*, 2010, **45**, 1912–1915.

13 M. Lippi, P. Rossi, J. Ceccarelli, S. Milazzo, J. M. Missina, A. Ienco and P. Paoli, The same but not the same: The case of (S)-naproxen/cis-1-amino-2-indanol chiral resolution via diastereomeric salt formation, *Cryst. Growth Des.*, 2024, **24**, 1658–1673.

14 P. Peluso and B. Chankvetadze, Recognition in the domain of molecular chirality: From noncovalent interactions to separation of enantiomers, *Chem. Rev.*, 2022, **122**, 13235–13400.

15 H. Yin, S. Xia, Z. Chen and S. Yuan, Insight into the role of hydroxypropyl cellulose in tuning crystallization behaviors of DL-methionine, *Chem Bio Eng.*, 2024, **1**, 704–714.

16 J. Sui, N. Wang, J. Wang, X. Huang, T. Wang, L. Zhou and H. Hao, Strategies for chiral separation: From racemate to enantiomer, *Chem. Sci.*, 2023, **14**, 11955–12003.

17 W. H. Lam and K. M. Ng, Diastereomeric salt crystallization synthesis for chiral resolution of ibuprofen, *AIChE J.*, 2007, **53**, 429–437.

18 P. Rossi, J. Ceccarelli, S. Milazzo, P. Paoli, J. Morais Missina, S. Ciattini, A. Lenco, G. Tuci, M. Valleri, M. P. Giovannoni, G. Guerrini and L. Conti, Nonsteroidal anti-inflammatory drugs-1-phenylethylamine diastereomeric salts: A systematic solid-state investigation, *Cryst. Growth Des.*, 2021, **21**, 6947–6960.

19 S. N. Angles, A. E. Miller and J. S. Johnson, Crystallization-induced diastereomer transformations of brominated arylacetic and arylpyruvic acids, *J. Org. Chem.*, 2025, **90**, 15921–15924.

20 M. Kitamura and K. Horimoto, Role of kinetic process in the solvent effect on crystallization of BPT propyl ester polymorph, *J. Cryst. Growth*, 2013, **373**, 151–155.

21 K. M. Brands and A. J. Davies, Crystallization-induced diastereomer transformations, *Chem. Rev.*, 2006, **106**, 2711–2733.

22 L. Addadi, S. Weinstein, E. Gati, I. Weissbuch and M. Lahav, Resolution of conglomerates with the assistance of tailor-made impurities. generality and mechanistic aspects of the "rule of reversal". A new method for assignment of absolute configuration, *J. Am. Chem. Soc.*, 1982, **104**, 4610–4617.

23 T. Hirose, K. Naito, M. Nakahara, H. Shitara, Y. Aoki, H. Nohira and B. W. Baldwin, New chiral kemp's acid diamides for chiral amine recognition by 1H NMR, *J. Inclusion Phenom. Macrocyclic Chem.*, 2002, **43**, 87–93.

24 K. Kinbara, Y. Kobayashi and K. Saigo, Chiral discrimination of 2-arylalkanoic acids by (1 S, 2 R)-1-aminoindan-2-ol through the formation of a consistent columnar supramolecular hydrogen-bond network, *J. Chem. Soc., Perkin Trans. 1*, 2000, **2**, 111–119.

25 J. J. Max and C. Chapados, Infrared spectroscopy of aqueous carboxylic acids: Comparison between different acids and their salts, *J. Phys. Chem. A*, 2004, **108**, 3324–3337.

26 L. F. Diniz, M. S. Souza, P. S. Carvalho Jr, C. C. da Silva, R. F. D'Vries and J. Ellena, Novel Isoniazid cocrystals with aromatic carboxylic acids: Crystal engineering, spectroscopy and thermochemical investigations, *J. Mol. Struct.*, 2018, **1153**, 58–68.

27 A. J. Cruz-Cabeza and J. Bernstein, Conformational polymorphism, *Chem. Rev.*, 2014, **114**, 2170–2191.

28 C. Brandel, Y. Amharar, J. M. Rollinger, U. J. Griesser, Y. Cartigny, S. Petit and G. Coquerel, Impact of molecular flexibility on double polymorphism, solid solutions and chiral discrimination during crystallization of diprophylline enantiomers, *Mol. Pharmaceutics*, 2013, **10**, 3850–3861.

29 J. E. Carpenter and M. Grunwald, Pre-nucleation clusters predict crystal structures in models of chiral molecules, *J. Am. Chem. Soc.*, 2021, **143**, 21580–21593.

30 T. Lu, Visualization analysis of covalent and noncovalent interactions in real space, *Angew. Chem., Int. Ed.*, 2025, **64**, e202504895.

31 K. Zhou, J. Zhang, Y. Geng, P. Gao, Y. Xie, J. Dong and W. Gong, Water-resistant, scalable, and inexpensive chiral metal-organic framework featuring global negative electrostatic potentials for efficient acetylene separation, *Chem Bio Eng.*, 2024, **1**, 349–356.

32 J. Li, H. Cheng and Z. Qi, Enhancement of separation performance for ofloxacin enantiomers by a biphasic recognition chiral extraction system, *AIChE J.*, 2024, **70**, e18367.

33 G. Preda, S. La Cognata, L. Pedraza-González, L. Carlier, M. Kolb, G. Pescitelli, V. Amendola, D. Armspach and D. Pasini, Manipulating stereo-communication in binaphthol-bridged α-and β-cyclodextrins to develop β-selective chiroptical pH switching and anion sensing in water, *Org. Chem. Front.*, 2025, **12**, 6450–6459.

34 F. L. Mota, A. J. Queimada, S. P. Pinho and E. A. Macedo, Aqueous solubility of some natural phenolic compounds, *Ind. Eng. Chem. Res.*, 2008, **47**, 5182–5189.

35 M. Simon, P. Donnellan, B. Glennon and R. C. Jones, Resolution via diastereomeric salt crystallization of ibuprofen lysine: Ternary phase diagram studies, *Chem. Eng. Technol.*, 2018, **41**, 921–927.

36 T. Lu, *Molclus program. Version 1.12*, http://www.keinsci.com/research/molclus.html, (accessed August 2023).

37 J. J. Stewart, MOPAC: A semiempirical molecular orbital program, *J. Comput.-Aided Mol. Des.*, 1990, **4**, 1–103.

38 M. J. Frisch, G. W. Trucks, H. B. Schlegel, G. E. Scuseria, M. A. Robb, J. R. Cheeseman, G. Scalmani, V. Barone, G. A. Petersson, H. Nakatsuji, X. Li, M. Caricato, A. V. Marenich, J. Bloino, B. G. Janesko, R. Gomperts, B. Mennucci, H. P. Hratchian, J. V. Ortiz, A. F. Izmaylov, J. L. Sonnenberg, D. Williams-Young, F. Ding, F. Lipparini, F. Egidi, J. Goings, B. Peng, A. Petrone, T. Henderson, D. Ranasinghe, V. G. Zakrzewski, J. Gao, N. Rega, G. Zheng, W. Liang, M. Hada, M. Ehara, K. Toyota, R. Fukuda, J. Hasegawa, M. Ishida, T. Nakajima, Y. Honda, O. Kitao, H. Nakai, T. Vreven, K. Throssell, J. A. Montgomery Jr., J. E. Peralta, F. Ogliaro, M. J. Bearpark, J. J. Heyd, E. N. Brothers, K. N. Kudin, V. N. Staroverov, T. A. Keith, R. Kobayashi, J. Normand, K. Raghavachari, A. P. Rendell, J. C. Burant, S. S. Iyengar, J. Tomasi, M. Cossi, J. M. Millam, M. Klene, C. Adamo, R. Cammi, J. W. Ochterski, R. L. Martin, K. Morokuma, O. Farkas, J. B. Foresman and D. J. Fox, *Gaussian 16, Revision B.01*, Gaussian, Inc., Wallingford, CT, 2016.

39 S. Grimme, S. Ehrlich and L. Goerigk, Effect of the damping function in dispersion corrected density functional theory, *J. Comput. Chem.*, 2011, **32**, 1456–1465.

40 T. Lu and F. Chen, Multiwfn: A multifunctional wavefunction analyzer, *J. Comput. Chem.*, 2012, **33**, 580–592.

41 P. R. Spackman, M. J. Turner, J. J. McKinnon, S. K. Wolff, D. J. Grimwood, D. Jayatilaka and M. A. Spackman, CrystalExplorer: A program for Hirshfeld surface analysis, visualization and quantitative analysis of molecular crystals, *J. Appl. Crystallogr.*, 2021, **54**, 1006–1011.

42 D. Van Der Spoel, E. Lindahl, B. Hess, G. Groenhof, A. E. Mark and H. J. Berendsen, GROMACS: Fast, flexible, and free, *J. Comput. Chem.*, 2005, **26**, 1701–1718.

43 T. Lu, *Sobtop, Version 1.0(dev5)*, http://sobereva.com/soft/Sobtop, (accessed March 2025).

44 (*a*) CCDC 2491484: Experimental Crystal Structure Determination, 2026, DOI: 10.5517/ccdc.csd.cc2pmlgd; (*b*) CCDC 2491485: Experimental Crystal Structure Determination, 2026, DOI: 10.5517/ccdc.csd.cc2pmlhf; (*c*) CCDC 2491489: Experimental Crystal Structure Determination, 2026, DOI: 10.5517/ccdc.csd.cc2pmlmk; (*d*) CCDC 2491490: Experimental Crystal Structure Determination, 2026, DOI: 10.5517/ccdc.csd.cc2pmlnl; (*e*) CCDC 2491491: Experimental Crystal Structure Determination, 2026, DOI: 10.5517/ccdc.csd.cc2pmlpm.